Applied Catalysis B: Environmental 196 (2016) 16–26

Contents lists available at ScienceDirect

Applied Catalysis B: Environmental

journal homepage: www.elsevier.com/locate/apcatb

Sol-gel-derived, $CaZrO_3$-stabilized Ni/CaO-$CaZrO_3$ bifunctional catalyst for sorption-enhanced steam methane reforming

Changjun Zhao [a], Zhiming Zhou [a,*], Zhenmin Cheng [a], Xiangchen Fang [b,*]

[a] State Key Laboratory of Chemical Engineering, East China University of Science and Technology, Shanghai 200237, China
[b] Fushun Research Institute of Petroleum and Petrochemicals, SINOPEC, Fushun 113001, China

ARTICLE INFO

Article history:
Received 15 February 2016
Received in revised form 14 April 2016
Accepted 11 May 2016
Available online 11 May 2016

Keywords:
Sorption-enhanced steam methane reforming
Bifunctional catalyst
Structure-activity relationship
CO_2 capture
Hydrogen

ABSTRACT

Sorption-enhanced steam methane reforming (SESMR) that combines steam reforming of methane with in situ CO_2 removal is a promising technology for H_2 production, and bifunctional catalysts that integrate catalytic and absorptive sites into one body are believed to have reduced mass transfer resistances. However, it is still a challenge to prepare bifunctional catalysts with high stability. Here, we used a sol-gel technique based on the formation of citrate complexes to prepare a series of Ni/CaO-$CaZrO_3$ bifunctional catalysts in which Ni, CaO and $CaZrO_3$ acted as catalyst, sorbent and stabilizer, respectively. The stabilizer, Ni loading and CaO content had a direct effect on the structure and morphology of the catalyst, which in turn influenced its CO_2 uptake and SESMR performance. Compared to Ni/CaO, the $CaZrO_3$-stabilized Ni/CaO-$CaZrO_3$ had smaller and fluffier grains, showing not only higher CO_2 uptake and better stability in 50 carbonation-calcination cycles, but also higher stability during cyclic SESMR process. In particular, the catalyst with a Ni loading of 15wt%, CaO content of around 60wt% and $CaZrO_3$ content of 25wt% presented the best SESMR performance by taking into account the catalytic activity and stability as well as the duration of the prebreakthrough period. However, the best catalyst was still subject to slow deactivation during a long-term stability test (up to 90 SESMR cycles), which was mostly due to the smooth and compact shell formed on the catalyst surface. The partially deactivated catalyst can be effectively reactivated by an additional carbonation step during the cyclic SESMR operation.

1. Introduction

As a promising technology for hydrogen production, the sorption-enhanced steam methane reforming process (SESMR) that integrates steam methane reforming (SMR, Eqs. (1) and (2)), water-gas shift (WGS, Eq. (3)) and in situ CO_2 separation (Eq. (4), using CaO as an example) presents substantial advantages (e.g., increased conversion of CH_4 and yield of H_2, simplified procedure, low investment cost, improved process efficiency, etc.) over the traditional SMR process, and thus has received much attention during the last two decades [1–4].

$$CH_4 + H_2O \leftrightarrow CO + 3H_2,\ \Delta H_{20^oC} = 205.7\text{kJ/mol} \quad (1)$$

$$CH_4 + 2H_2O \leftrightarrow CO_2 + 4H_2,\ \Delta H_{20^oC} = 164.5\ \text{kJ/mol} \quad (2)$$

$$CO + H_2O \leftrightarrow CO_2 + H_2,\ \Delta H_{20^oC} = -41.2\text{kJ/mol} \quad (3)$$

$$CaO + CO_2 \leftrightarrow CaCO_3,\ \Delta H_{20^oC} = -178.2\text{kJ/mol} \quad (4)$$

To date, most of the investigations on the SESMR can be classified into two categories in terms of the ways in which catalyst and sorbent are employed. In the first category, catalytic and absorptive sites are separately located on two types of particles, i.e., catalyst and sorbent are two different particles and they are homogenously mixed [5–13] or multi-section packed [14–16] in the reactor. In the second category, however, catalytic and absorptive sites are integrated into one particle, namely hybrid or bifunctional catalyst [17–26]. Theoretical investigations [27–31] have demonstrated that the bifunctional catalyst can reduce the mass transfer limitations and improve the utilization efficiency of the absorptive sites compared to the physical mixture of catalyst and sorbent, which is also confirmed by experimental studies [32,33].

Among all the possible bifunctional catalysts for the SESMR, CaO is the most investigated absorptive material due to its wide availability, low cost, high CO_2 uptake and fast carbonation rate. Although many investigations have been performed on the CaO-based bifunctional catalysts, there are still some important issues that need to be addressed. The first issue is the catalyst stability.

* Corresponding authors.
E-mail addresses: zmzhou@ecust.edu.cn, michaelzmzhou@gmail.com (Z. Zhou), fangxiangchen.fshy@sinopec.com (X. Fang).

http://dx.doi.org/10.1016/j.apcatb.2016.05.021
0926-3373/

On the one hand, some researchers [18,19,26] prepared bifunctional catalysts, which showed good activity in the SESMR, but unfortunately these catalysts were evaluated only for one cycle and their stability in multiple cycles was unclear. On the other hand, the cyclic stability (at least 10 cycles) of bifunctional catalyst was assessed in some studies [20,21,23,32], but the results were unsatisfactory, as the catalytic activities of these catalysts decreased without exception during the cyclic operation. Recently, we prepared a Ni/CaO-$Ca_5Al_6O_{14}$ catalyst that exhibited a good stability in 50 SESMR cycles [24]; however, a slow loss in activity was still observed over extended cycles of operation. It seems that the loss in activity of bifunctional catalyst inevitably occurs after a certain number of cycles which depend on the catalyst and reaction conditions. This situation brings about the second issue: how if possible to reactivate the deactivated bifunctional catalyst? To the best of our knowledge, no relevant literature is available in this field despite the fact that some researches have been devoted to the development of various strategies designed for the reactivation of spent CaO-based CO_2 sorbents [34–37].

In this work, $CaZrO_3$-stabilized Ni/CaO-$CaZrO_3$ bifunctional catalysts were prepared by a simple sol-gel method and applied to the SESMR process. First, the effects of Ni loading and CaO content on the structure and activity of the catalysts were examined by various analysis techniques, multiple carbonation-calcination cycles in a thermogravimetric analyzer (TGA) and cyclic SESMR in a fixed-bed reactor. Second, a screened bifunctional catalyst was evaluated in a long-term SESMR operation (up to 90 cycles), and the deactivation mechanism of the catalyst was discussed. Third, some possible approaches were explored to reactivate the partially deactivated catalyst. The findings of this study will facilitate the design and preparation of "catalyst-sorbent" bifunctional catalysts for the SESMR process.

2. Experimental

2.1. Catalyst preparation

A series of bifunctional catalysts with different Ni loading and CaO content were prepared by sol-gel method using citric acid as a metal-complex agent. First, a certain amount of calcium nitrate tetrahydrate, zirconium nitrate pentahydrate, nickel nitrate hexahydrate and citric acid monohydrate (the molar ratio of citric acid to cation (Ca^{2+}, Zr^{4+} and Ni^{2+}) was 1.2) were dissolved in deionized water (the molar ratio between water and citric acid amounted to 50) and the pH value of the mixed solution was adjusted to 1–2 by nitric acid, after which the solution was heated to 80 °C with vigorous stirring under reflux and continued for 2 h. Next, a predetermined amount of polyethylene glycol with a molecular weight of 300 (the mass ratio of polyethylene glycol to citric acid was 0.5) was added, and the mixed solution was continuously stirred under reflux for 6 h at 105 °C. Finally, the formed gel was dried for 12 h in an oven at 110 °C and ground into a fine powder, which was further calcined for 2 h in a muffle furnace at 850 °C with a heating rate of 5 °C/min.

The Ni loading and CaO content of the bifunctional catalysts can be tuned by adjusting the amount of each metal precursor in the initial solution. The nominal CaO/ZrO_2 mass ratio for all catalysts was fixed at 4 because our previous study had shown that the CaO-based sorbent with such a ratio possessed high CO_2 uptake and good stability during cyclic CO_2 capture [38]. It should be noted that the content of free CaO in the catalyst can only be determined after identification of the crystalline structure of all phases in the sample, which will be discussed later. The as-prepared catalyst is denoted as Nix/CaZr, where x represents the Ni loading of the catalyst. For comparison, a Ni15/CaO catalyst without addition of zirconium was also prepared by the above procedure.

2.2. Catalyst characterization

Brunauer-Emmett-Teller (BET) surface area, pore volume and average pore diameter of the catalyst were measured by N_2 adsorption-desorption at −196 °C using a Micromeritics ASAP 2010 equipment. Before measurement the sample was degassed at 133.3 Pa and 150 °C for 6 h. The crystalline structure of the catalyst was obtained by X-ray diffraction (XRD, Rigaku D/Max 2550) using Cu Kα radiation with wavelength of 1.54056 Å. The data were collected over a 2θ range of 10–80° with a step size of 0.02°. The element concentrations of the catalyst were measured by inductively coupled plasma-optical emission spectroscopy (ICP-OES, Varian 710ES). Temperature programmed reduction (TPR, Micromeritics AutoChem 2920) was carried out in a stream of H_2/Ar (10/90, v/v) at a flow rate of 30 mL/min, from room temperature to 750 °C with a heating rate of 10 °C/min, and the H_2 consumption was monitored by a thermal conductivity detector (TCD). The nickel surface area of the catalyst and the corresponding metal dispersion were determined by H_2 chemisorption (Micromeritics AutoChem 2920). The weighted catalyst was first reduced under a flow of 30 mL/min of 10% H_2/Ar at 700 °C for 2 h, and then the reactor was purged with Ar at 730 °C for 30 min to remove H_2. After cooling to 35 °C in Ar, H_2 pulse chemisorption (0.5 mL each) started. The measured H_2 uptake was used to calculate the surface Ni and its dispersion assuming a H:Ni stoichiometry factor of 1. The morphology of the catalyst was observed by field emission scanning electron microscopy (FESEM, Nova NanoSEM 450) and high-resolution transmission electron microscopy (HRTEM, JEOL JEM-2100), and the local elemental analysis of the catalyst was performed using an energy dispersive spectrometer (EDS, EDAX Genesis XM2 system) attached to HRTEM. The sample for HRTEM analysis was sonicated in ethanol for 30 min and subsequently deposited onto a carbon-coated cooper grid. The surface of the bifunctional catalyst was examined by X-ray photoelectron spectroscopy (XPS, Thermo Scientific ESCALAB 250Xi) using Al Kα radiation ($h\nu$ = 1486.6 eV) and a pass energy of 40 eV, and all the binding energies were calibrated to the C1s peak at 284.8 eV of the surface adventitious carbon.

2.3. Catalyst test

The catalytic activity of bifunctional catalysts for SESMR and their CO_2 capture capacity were evaluated in a fixed-bed quartz tube reactor (16 mm i.d.) and a TGA (WRT-3P, Shanghai Precision & Scientific Instrument Co., Ltd), respectively. In the fixed-bed reactor, 4 g of catalyst (50–75 μm) diluted with quartz sand (1/1, v/v) was positioned in the middle of the reactor and reduced by a flow of 40% H_2 in N_2 (100 mL/min). The reduction temperature was programmed to increase from room temperature to 700 °C at a heating rate of 5 °C/min and to hold for 2 h at 700 °C. The product gas after removal of steam was analyzed online by a gas chromatograph (HP 6890) equipped with a TCD. Detailed information on the experimental setup and the analysis method was presented elsewhere [11]. In the SESMR experiments, except where specified otherwise, the reforming reaction was conducted at 600 °C and 1 bar for about 2 h with an inlet CH_4 flow rate of 16.6 mL/min and a H_2O/CH_4 molar ratio of 3, while the catalyst regeneration was carried out at 800 °C and 1 bar for 1 h with a N_2 flow of 100 mL/min. A temperature ramp rate of 10 °C/min was used between the two stages. In the TGA, about 5 mg of catalyst (50–75 μm) was placed in a platinum basket and the catalyst weight was continuously recorded during the carbonation-calcination cyclic operation. Carbonation was performed at 650 °C for 20 min in 15% CO_2/85% N_2, and calcination at 800 °C for 10 min in pure N_2. The total gas flow rate was maintained

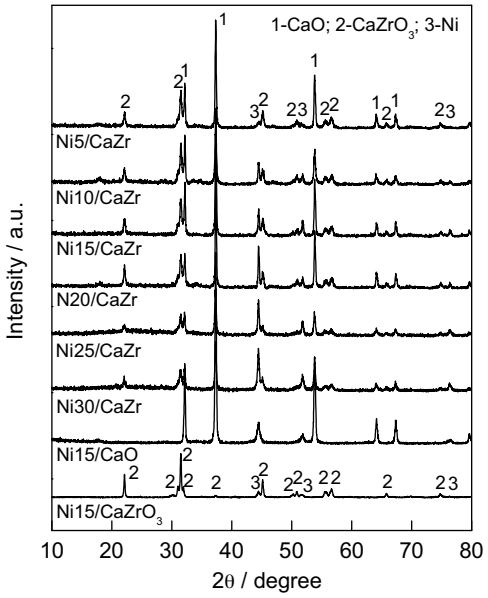

Fig. 1. XRD patterns of reduced Nix/CaZr catalysts.

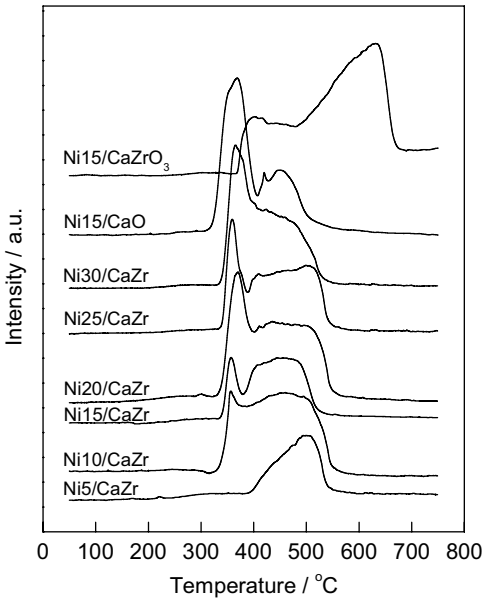

Fig. 2. TPR profiles of Nix/CaZr catalysts.

at 50 mL/min and the temperature ramp rate between carbonation and calcination was 10 °C/min.

3. Results and discussion

3.1. Physicochemical properties of bifunctional catalysts

Table 1 lists the ICP-OES measured Ni, Ca and Zr concentrations of unreduced catalysts as well as the corresponding theoretical concentrations. There is almost no difference between measured and calculated values over all the catalysts, which is reasonable due to the method used for catalyst preparation that ensures no loss of Ni, Ca and Zr during the preparation process. Fig. 1 shows the XRD patterns of reduced Nix/CaZr catalysts. All the catalysts consist of Ni (JCPDS 87-0712), CaO (JCPDS 77-2012) and $CaZrO_3$ (JCPDS 35-0790), and no diffraction peaks assigned to ZrO_2 are observed, implying that all of ZrO_2 has reacted with a part of CaO to form $CaZrO_3$ during high-temperature calcination of the catalysts. This is also evidenced by the XRD pattern of $Ni15/CaZrO_3$ prepared by the same procedure with a Ca:Zr precursor molar ratio of 1:1, which is equal to the stoichiometry expected from the equation of $CaO + ZrO_2 = CaZrO_3$. As shown in Fig. 1, $Ni15/CaZrO_3$ only contains Ni and $CaZrO_3$, but no ZrO_2. In general, with increasing the Ni loading, the peak intensity of the Ni phase increases, and the peak intensity of CaO and $CaZrO_3$ decreases. Based on the XRD patterns and the amount of metal precursors used during the catalyst preparation, the weight fractions of CaO and $CaZrO_3$ in the reduced Nix/CaZr can be calculated, which are listed in Table 1. The mass ratio of CaO to $CaZrO_3$ remains constant for all Nix/CaZr, being about 2.4.

Table 2 summarizes the BET surface area, pore volume and average pore diameter of different catalysts as well as the Ni surface area and Ni dispersion. There is no relation between the BET surface area (or pore volume or average pore diameter) and the Ni loading, in agreement with that reported by García-Lario et al. [25]. The Ni surface area of Nix/CaZr increases with the Ni loading up to 20wt% and then decreases, while the Ni dispersion generally decreases with the Ni loading. Among all the catalysts examined, Ni15/CaZr and Ni20/CaZr have the largest Ni surface area.

Fig. 2 presents the H_2-TPR profiles of fresh Nix/CaZr catalysts. There are two main reduction peaks for Ni15/CaO. The first peak located at about 360 °C could be ascribed to the reduction of NiO species weakly interacted with CaO, and the second (a hump at around 450 °C) corresponds to the NiO species with a strong interaction with CaO [24,39]. Similarly, two reduction peaks are noticed for $Ni15/CaZrO_3$, but with higher temperatures than those of Ni/CaO. The first peak at 400 °C and the second peak at 630 °C are attributed, respectively, to the weak and strong NiO-$CaZrO_3$ interaction. Different from Ni15/CaO and $Ni15/CaZrO_3$, for the case of Nix/CaZr, NiO can be supported not only on the surface of CaO but also on the surface of $CaZrO_3$. As shown in Fig. 2, most Nix/CaZr catalysts except Ni5/CaZr display a distinct reduction peak at around 360 °C together with a hump between 380 and 550 °C, while for Ni5/CaZr the first peak is absent. The first reduction peak of Nix/CaZr ($x \geq 10$) can be ascribed, similar to Ni15/CaO, to NiO having a weak interaction with CaO, but the second one is ascribed not only to the reduction of NiO with strong NiO-CaO interaction, but also to the reduction of NiO crystallites supported on $CaZrO_3$. This is because: (I) the temperature of the second reduction peak of Nix/CaZr is higher than that of Ni15/CaO but lower than that of $Ni15/CaZrO_3$, indicating the synergistic effect of CaO and $CaZrO_3$; and (II) with increasing the Ni loading, the second reduction peak of Nix/CaZr becomes weaker, which is in line with the decreased amount of $CaZrO_3$ in the catalyst.

Fig. 3 shows the FESEM images of some Nix/CaZr catalysts. It is clear that Ni5/CaZr, Ni15/CaZr and Ni30/CaZr possess smaller and fluffier grains than Ni15/CaO. In addition, the grain size of Nix/CaZr gradually increases with an increase in the Ni loading or a decrease in the amount of $CaZrO_3$. The morphology variation with the content of $CaZrO_3$ implies that $CaZrO_3$ has the effect of dispersing NiO particles and separating CaO grains. Fig. 4 displays the HRTEM images of Nix/CaZr, from which the Ni particle size of the catalyst is analyzed and listed in Table 2. It appears that the average Ni particle size increases in general with increasing the Ni loading or decreasing the amount of $CaZrO_3$, which is correlated well with the variation of the Ni dispersion of Nix/CaZr catalysts. Moreover, the catalyst with a relatively lower amount of $CaZrO_3$, such as Ni25/CaZr and Ni30/CaZr, exhibits a wider Ni particle size distribution (PSD), and as an extreme case, Ni15/CaO without $CaZrO_3$ has the widest Ni PSD. All these observations indicate the beneficial effect of $CaZrO_3$ promotion.

Table 1
Catalyst composition of Nix/CaZr.

Catalyst	Metal concentration[a] (wt%)			Composition[b] (wt%)		
	Ni	Ca	Zr	Ni	CaO	$CaZrO_3$
Ni5/CaZr	5.1 (5)	53.2 (53.5)	14.1 (13.9)	5	67.4	27.6
Ni10/CaZr	9.8 (10)	51.3 (49.9)	12.7 (12.9)	10	63.8	26.2
Ni15/CaZr	15.2 (15)	46.5 (46.3)	11.8 (12.0)	15	60.3	24.7
Ni20/CaZr	19.7 (20)	42.9 (42.6)	11.4 (11.0)	20	56.7	23.3
Ni25/CaZr	24.6 (25)	38.7 (39.0)	10.3 (10.1)	25	53.2	21.8
Ni30/CaZr	30.3 (30)	35.6 (35.4)	9.0 (9.2)	30	49.6	20.4
Ni15/CaO	14.8 (15)	58.1 (57.8)	–	15	85	–

[a] Measured and calculated metal concentrations of unreduced catalysts are given by the values outside and inside the brackets, respectively.
[b] Theoretical composition of reduced catalysts calculated from the amount of precursors used.

Table 2
Textural properties of Nix/CaZr catalysts.

Catalyst	S_{BET} (m^2/g_{cat})	V_{pore} (cm^3/g_{cat})	d_{pore}[a] (nm)	S_{Ni}[b] (m^2/g_{cat})	D_{Ni}[c] (%)	d_{Ni}[d] (nm)
Ni5/CaZr	14.7	0.075	18.0	0.31	0.94	19.3 ± 2.6
Ni10/CaZr	19.4	0.111	22.4	0.64	0.96	19.7 ± 3.1
Ni15/CaZr	12.8	0.097	28.6	0.90	0.90	19.2 ± 1.5
Ni20/CaZr	13.1	0.090	41.4	0.92	0.69	20.3 ± 1.6
Ni25/CaZr	21.7	0.132	23.1	0.84	0.51	20.5 ± 5.2
Ni30/CaZr	12.5	0.073	40.2	0.78	0.39	22.5 ± 5.4
Ni15/CaO	23.5	0.163	28.4	0.86	0.86	19.4 ± 6.3

[a] BJH pore diameter determined from the adsorption branch.
[b] Nickel surface area measured from H_2 chemisorption.
[c] Nickel dispersion obtained from H_2 chemisorption.
[d] Nickel particle size acquired from HRTEM images.

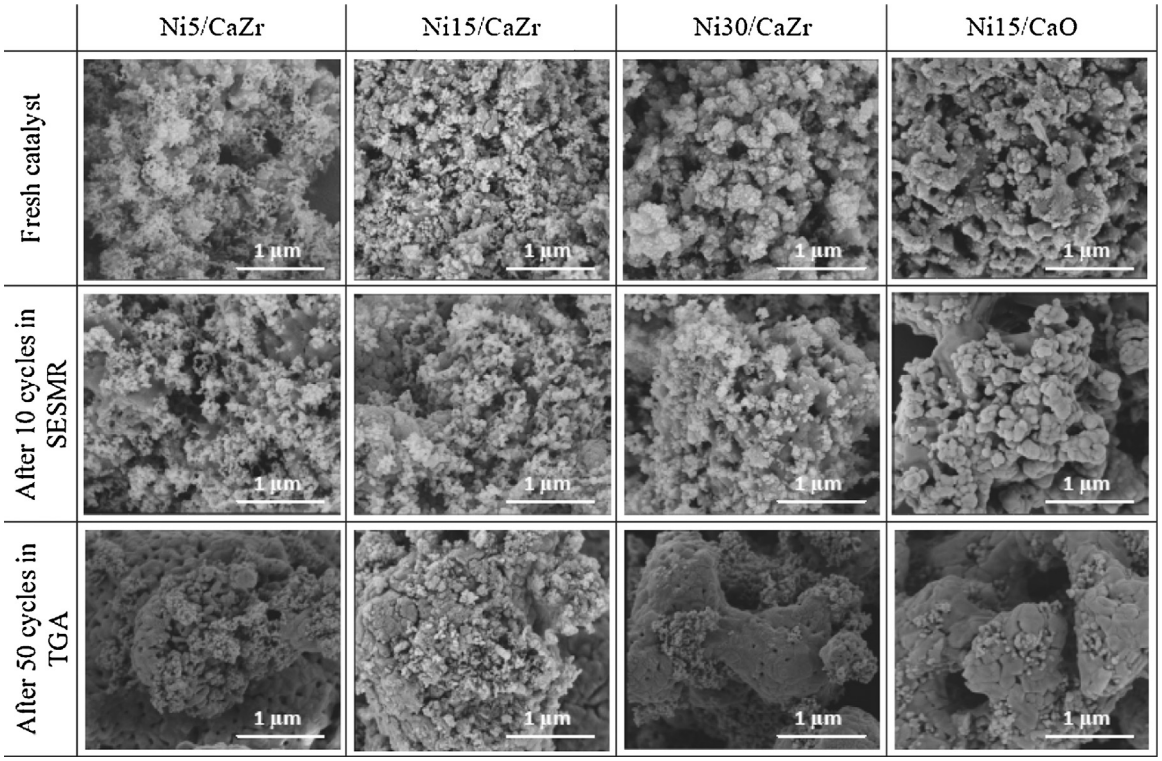

Fig. 3. FESEM images of fresh and used Nix/CaZr catalysts: fresh (up row), calcined after 10 cycles in SESMR (middle row), and calcined after 50 cycles in TGA (down row).

Fig. 5 shows the element distribution of Ni, Ca and Zr in some Nix/CaZr catalysts. For Ni5/CaZr and Ni15/CaZr each element is homogeneously distributed in the catalyst, but for Ni30/CaZr the element distribution is inhomogeneous, e.g., zone A is rich in Ca but poor in Zr and Ni. The inhomogeneous element distribution of Ni30/CaZr is probably related to its relatively low $CaZrO_3$ content. Further observations on Ni30/CaZr reveal that the Zr-rich area (zone B) has a denser distribution of Ni than the Ca-rich area (zone A), implying that $CaZrO_3$ has a higher affinity for Ni than CaO. This is also the reason why the reduction peak corresponding to the weak NiO-CaO interaction is missing for Ni5/CaZr (Fig. 2), since most nickel species are preferentially supported on the surface of $CaZrO_3$. Similarly, previous studies have demonstrated that Ni has a high affinity to $Ca_{12}Al_{14}O_{33}$ [18] and $Ca_5Al_6O_{14}$ [24]. With

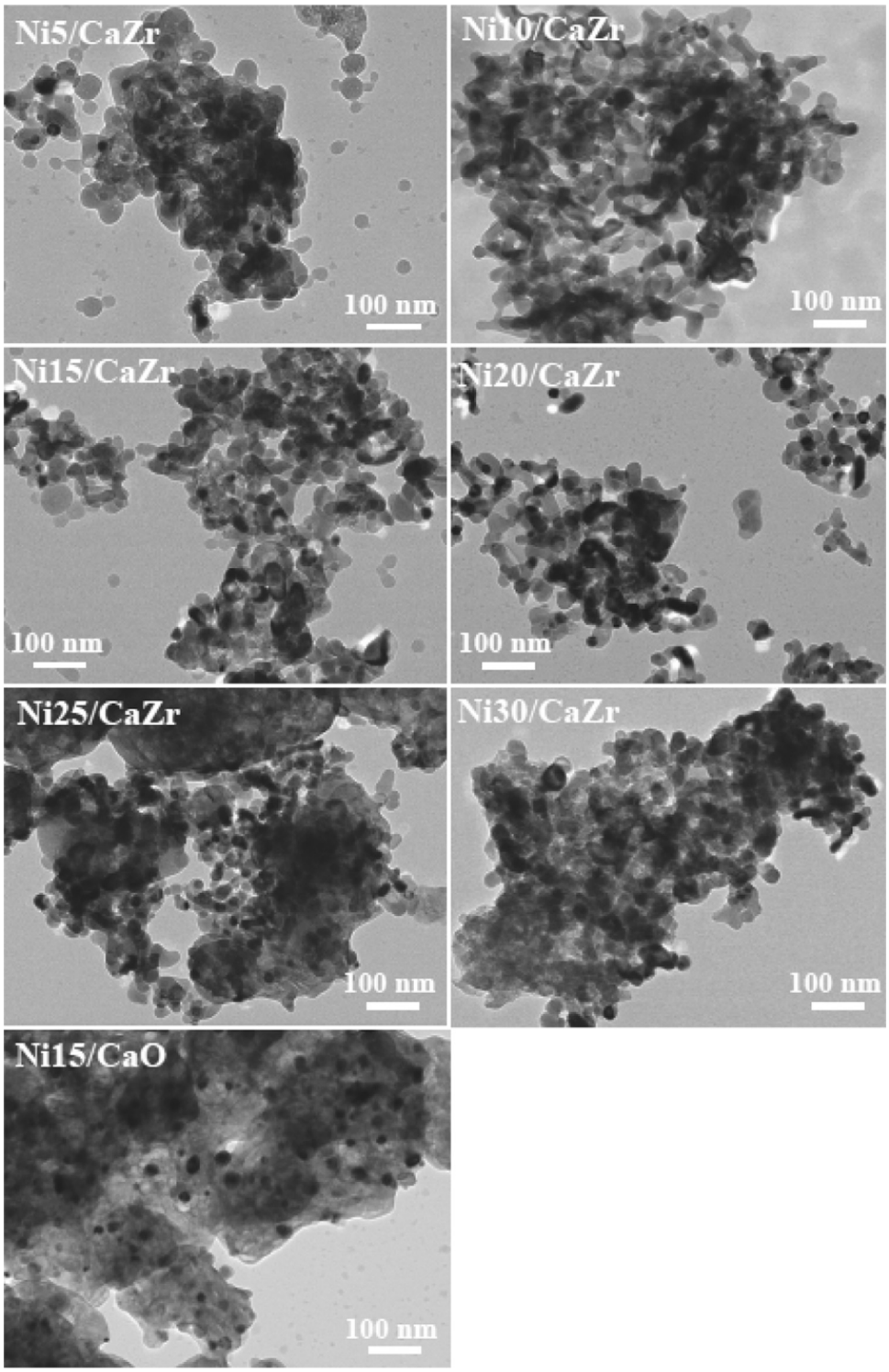

Fig. 4. HRTEM images of reduced Nix/CaZr catalysts.

increasing the Ni loading and decreasing the $CaZrO_3$ content, the amount of $CaZrO_3$ is insufficient to disperse all of NiO particles and some particles have to be immobilized on the surface of CaO. Therefore, as shown in Fig. 2, the first reduction peak of Nix/CaZr gradually intensifies with increasing x.

3.2. CO_2 uptake of bifunctional catalysts

Fifty carbonation-calcination cycles are carried out in the TGA to compare the CO_2 capture performance of different bifunctional catalysts. As shown in Fig. 6, all Nix/CaZr catalysts have higher CO_2 uptake (mass of CO_2 absorbed per unit mass of catalyst instead of CaO) and better stability than Ni15/CaO, highlighting the stabilization effect of $CaZrO_3$. Corresponding to Ni15/CaO, Ni5/CaZr, Ni10/CaZr, Ni15/CaZr, Ni20/CaZr, Ni25/CaZr and Ni30/CaZr, the average decay rates over 50 cycles are calculated to be 0.80, 0.21, 0.32, 0.21, 0.30, 0.39 and 0.33%/cycle, respectively. Apparently, Ni5/CaZr and Ni15/CaZr have the best cyclic stability among all the catalysts tested in this study. The decay in the CO_2 uptake is usually associated with the variation of the sorbent morphology [3,40]. As

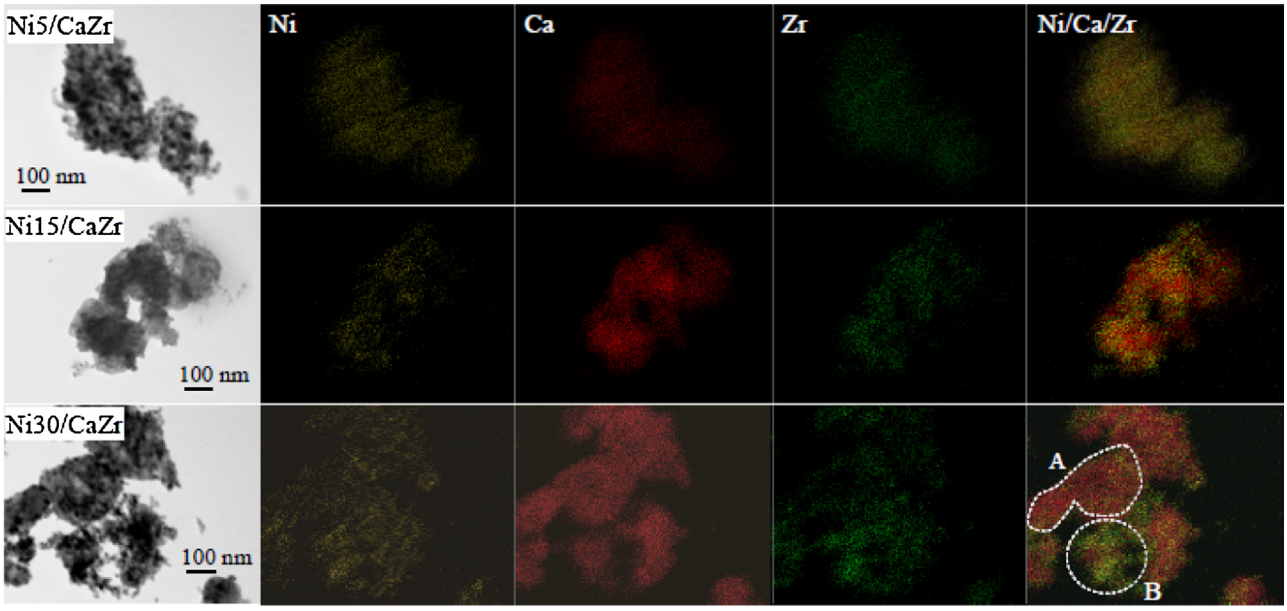

Fig. 5. EDS mapping of reduced Ni5/CaZr, Ni15/CaZr and Ni30/CaZr catalysts.

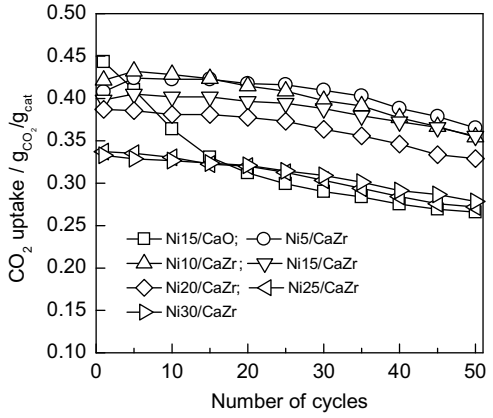

Fig. 6. CO_2 uptake of Nix/CaZr catalysts over 50 carbonation-calcination cycles. Carbonation: 650 °C, 20 min, 15% CO_2/85% N_2; calcination: 800 °C, 10 min, pure N_2; temperature ramp rate of 10 °C/min.

observed from Fig. 3, after 50 consecutive cycles, sintering of CaO particles inevitably occurs, resulting in a loss of CO_2 capture capacity of bifunctional catalysts. Nevertheless, the used Ni5/CaZr and Ni15/CaZr still possess much more small grains and interconnected pore networks than Ni30/CaZr and Ni15/CaO, in accordance with their cyclic stability.

An interesting observation is that the self-reactivation phenomenon (the CO_2 uptake of sorbent increases with cycling during the first several cycles) [41–43] is present for those catalysts with relatively lower Ni loading and higher CaO content, including Ni5/CaZr, Ni10/CaZr and Ni15/CaZr, but not for Ni20/CaZr, Ni25/CaZr and Ni30/CaZr. The self-reactivation is normally caused by a competition between two factors: one is an increase in the pore volume of regenerated sorbent achieved after calcination or decarbonation, which is favorable for CO_2 uptake, and the other is sintering of CaO particles, which is adverse for CO_2 absorption [42]. The competition between them leads to either an increase in the CO_2 uptake if the advantages supplied by the increased pore volume outweigh the disadvantages from CaO sintering or a decrease if the former is inferior to the latter. The analysis as presented above has shown that for the catalyst with low Ni loading such

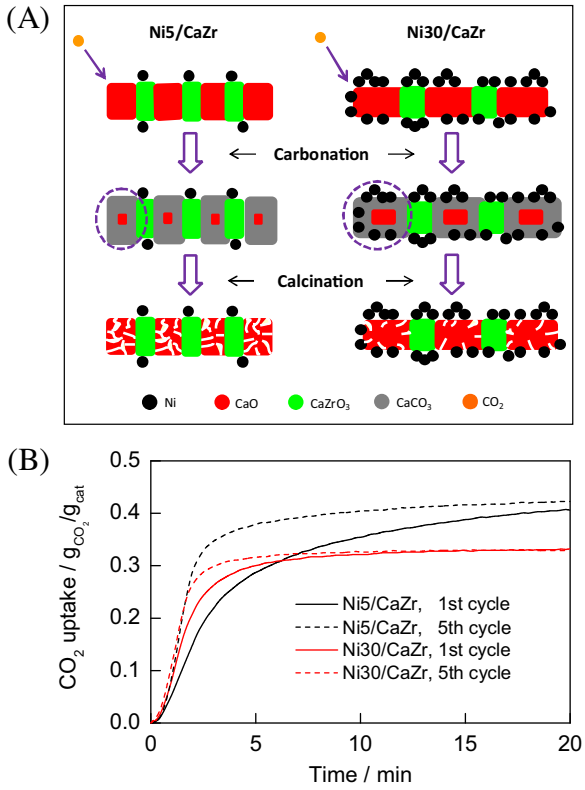

Fig. 7. (A) illustration of structural evolution and (B) CO_2 uptake of Nix/CaZr during initial cycles. Carbonation: 650 °C, 20 min, 15% CO_2/85% N_2; calcination: 800 °C, 10 min, pure N_2; temperature ramp rate of 10 °C/min.

as Ni5/CaZr, most nickel species is deposited on $CaZrO_3$ instead of CaO, which makes most of CaO accessible to CO_2. In addition, the small grains of Ni5/CaZr as well as its developed pore network are beneficial for CO_2 capture [44,45], which in turn can generate more pores/cracks inside the regenerated sorbent due to release of more CO_2 during calcination, as illustrated in Fig. 7(A). Indeed, even during the period of transition (from the fast surface reaction-controlled stage to the slow product layer diffusion-controlled

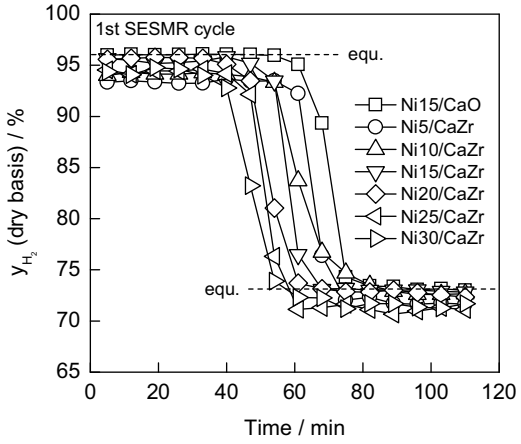

Fig. 8. Comparison of H_2 concentrations over different Nix/CaZr (the first SESMR cycle): catalyst (4 g), 600 °C, 1 bar, H_2O/CH_4 (molar ratio) = 3, $F_{CH_4,in}$ = 16.6 mL/min.

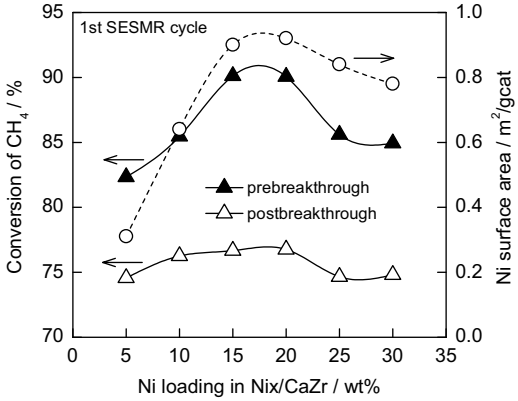

Fig. 9. Variation of CH_4 conversion with the Ni loading (the first SESMR cycle): catalyst (4 g), 600 °C, 1 bar, H_2O/CH_4 (molar ratio) = 3, $F_{CH_4,in}$ = 16.6 mL/min.

stage [46–48]), the fresh Ni5/CaZr (the first cycle) still absorbs CO_2 at a relatively high rate, as shown in Fig. 7(B), which contributes to the increased CO_2 uptake and consequently gives rise to the self-reactivation of Ni5/CaZr during the initial several cycles. On the contrary, for the case of Nix/CaZr with high Ni loading such as Ni30/CaZr, some nickel species supported on CaO may hinder to some extent the contact between CO_2 and CaO and thus increase the diffusion barrier of CO_2. The relatively large grains of Ni30/CaZr are also unfavorable for CO_2 uptake. Therefore, Ni30/CaZr exhibits a more rapid transition between the fast and slow stages when compared with Ni5/CaZr, and accordingly no self-reactivation is observed. The above analysis is further evidenced by N_2 adsorption analysis performed on 5-cycles used Ni5/CaZr and Ni30/CaZr. The pore volume of Ni5/CaZr increases from 0.075 cm^3/g (fresh) to 0.103 cm^3/g (5-cycles used), while for Ni30/CaZr the pore volume decreases from 0.073 to 0.058 cm^3/g. It should be noted that the five carbonation-calcination cyclic tests were carried out in a fixed-bed reactor due to the fact that the amount of sample used in the TGA (around 5 mg) was far insufficient for N_2 adsorption measurement. About 0.5 g of the catalyst was loaded into the reactor and the experimental conditions were the same as those in the TGA except that 100 mL/min of 15% CO_2/85% N_2 for carbonation and 100 mL/min of pure N_2 for calcination.

3.3. SESMR of bifunctional catalysts

Fig. 8 displays the typical concentration profiles of H_2 during the SESMR experiments and the data correspond to the first cycle. Three distinct regimes, i.e., prebreakthrough, breakthrough and postbreakthrough [10,21,24,25,49], are observed for all catalysts, and the duration of the prebreakthrough period at the first cycle depends as expected on the CaO content of the catalyst: the higher the CaO content, the longer is the prebreakthrough period. The dashed lines shown in Fig. 8 indicate the thermodynamic equilibrium concentrations of H_2 under the experimental condition investigated, being around 96% for the prebreakthrough period and 73% for the postbreakthrough period. It is obvious that the equilibrium concentrations are not attained by all catalysts and only Ni15/CaO, Ni15/CaZr and Ni20/CaZr can arrive at the equilibrium values. Fig. 9 further gives the variation of CH_4 conversion with the Ni loading in the Nix/CaZr catalyst. Likewise, only Ni15/CaZr and Ni20/CaZr are able to reach the equilibrium conversions of CH_4, which are about 91% and 77% for the prebreakthrough and postbreakthrough periods, respectively. Such observations can be rationalized in terms of the Ni surface area of Nix/CaZr (the dashed line in Fig. 9): Ni15/CaZr and Ni20/CaZr have the largest Ni surface

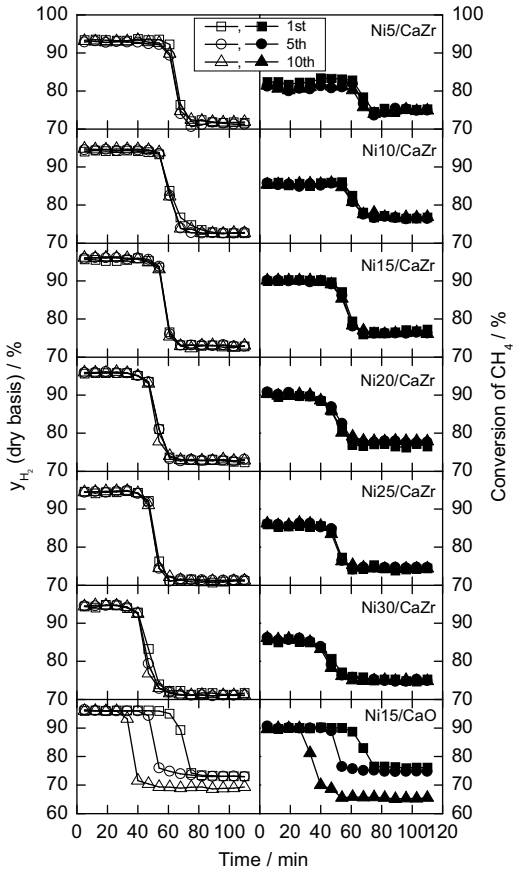

Fig. 10. H_2 Concentration and CH_4 conversion at the 1st, 5th and 10th SESMR cycles: catalyst (4 g), 600 °C, 1 bar, H_2O/CH_4 (molar ratio) = 3, $F_{CH_4,in}$ = 16.6 mL/min.

area that can ensure the equilibrium conversion of CH_4 for a given experimental condition, while the relatively lower Ni surface area of other Nix/CaZr is probably insufficient to realize this equilibrium conversion.

Fig. 10 shows the H_2 concentration profiles of different catalysts at the first, fifth and tenth cycles, and the corresponding conversions of CH_4 are also presented. All $CaZrO_3$-stabilized catalysts exhibit good stability during 10 consecutive SESMR cycles. In contrast, Ni15/CaO without $CaZrO_3$ gradually loses its activity with the number of cycles. The breakthrough period is shortened from 60 min at the first cycle to 47 min at the fifth cycle and further

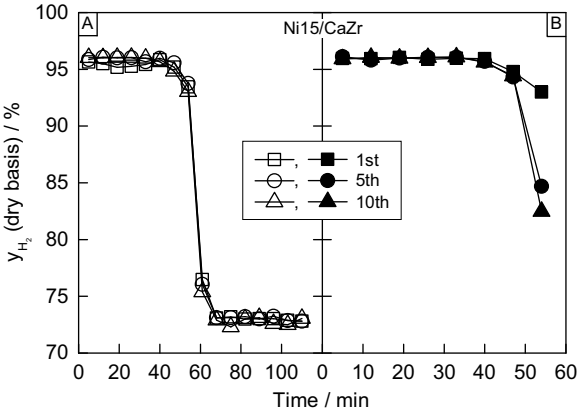

Fig. 11. Comparison of two different operation modes in the cyclic SESMR process: catalyst (4 g), 600 °C, 1 bar, H_2O/CH_4 (molar ratio) = 3, $F_{CH_4,in}$ = 16.6 mL/min.

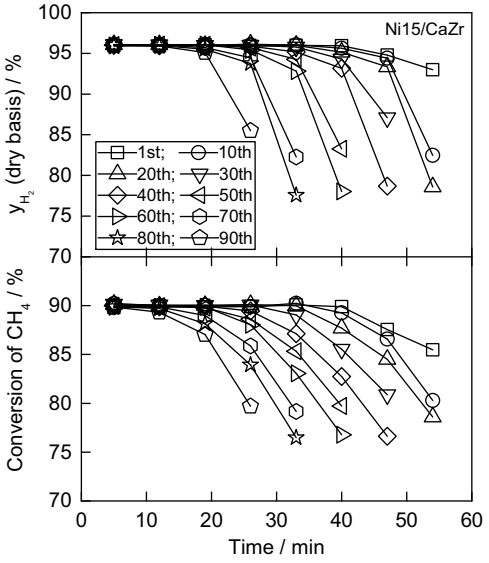

Fig. 12. H_2 concentration and CH_4 conversion over Ni15/CaZr during 90 SESMR cycles: catalyst (4 g), 600 °C, 1 bar, H_2O/CH_4 (molar ratio) = 3, $F_{CH_4,in}$ = 16.6 mL/min.

to 26 min at the tenth cycle. Moreover, both H_2 concentration (65%) and CH_4 conversion (69%) during the postbreakthrough period at the tenth cycle are lower than the equilibrium values, further indicating the stabilization effect of $CaZrO_3$. This effect can also been observed in the micrographs of used catalysts, as shown in Fig. 3. The morphologies of $CaZrO_3$-stabilized catalysts are still preserved after 10 SESMR cycles, especially for Ni5/CaZr and Ni15/CaZr, but sintering is clearly noticed for Ni15/CaO.

It should be noted that according to the experimental procedure described above (mode I), a complete SESMR cycle comprises three regimes (Figs. 8 and 10). Nevertheless, only the prebreakthrough period is of practical interest in that high conversion of CH_4 and high concentration of H_2 can be stably achieved during this period. Therefore, in the following section, the SESMR experiments are carried out in another mode (mode II) by the following procedure: the SMR reaction continues until the breakthrough period, and then SMR stops and the reaction system is heated up to 800 °C under pure N_2 for catalyst regeneration. Reaction and regeneration conditions for mode II are the same as those for mode I. Ni15/CaZr is chosen as the catalyst for the operation of mode II by taking into account its good activity and stability presented in mode I. The two operation modes, however, yield somewhat different results during the cyclic SESMR process. As shown in Fig. 11, in contrast with the high stability in mode I (Fig. 11(A)), the stability of Ni15/CaZr in mode II (Fig. 11(B)) slightly decreases. The H_2 concentrations at 54 min time on stream in mode II are about 93, 85 and 82% for the first, fifth and tenth cycles, respectively. The decreased stability of Ni15/CaZr in mode II is ascribed to the shortened reaction time, because an extended reaction time or carbonation time with regard to CaO is believed to increase the CaO utilization, i.e., a fraction of CaO that otherwise will not be utilized in a short time period can be transformed into $CaCO_3$, which in turn produces more active CaO for the next cycle upon calcination of the carbonated material [45,50,51].

In order to assess the long-term stability of Ni15/CaZr, 90 consecutive SESMR cycles are conducted according to mode II. It can be seen from Fig. 12 that with increasing the number of cycles the prebreakthrough period is gradually shortened, indicating that Ni15/CaZr is slowly deactivated, even though the H_2 concentration and conversion of CH_4 at the prebreakthrough period are still maintained at the equilibrium values. Different from no obvious sintering after only 10 cycles of operation (Fig. 3), sintering of Ni15/CaZr particles is present after 90 cycles. As presented in Fig. 13(A), aggregation and sintering of Ni15/CaZr result in a smooth and compact shell with few visible pores, which undoubt-

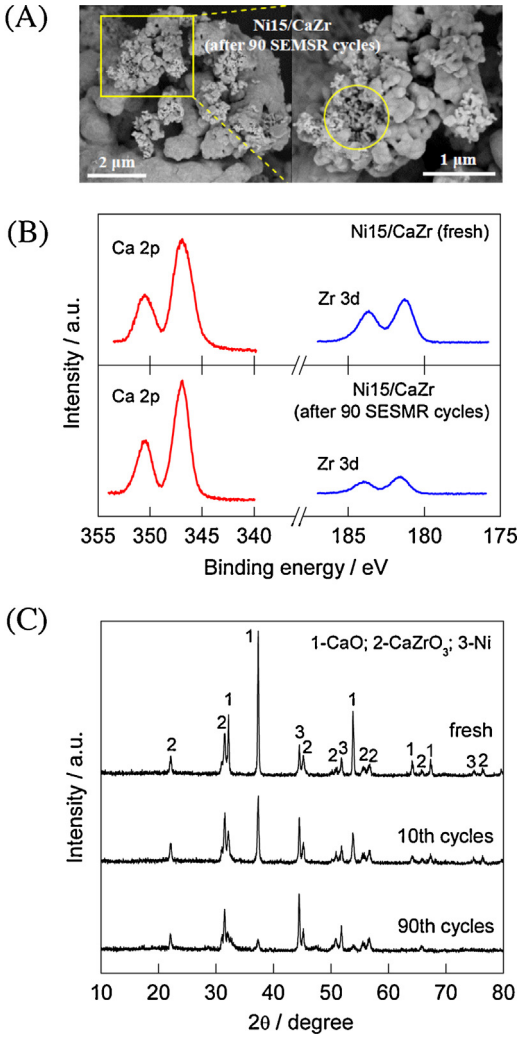

Fig. 13. 90-cycles used Ni15/CaZr: (A) HRTEM images; (B) XPS spectra; (C) XRD patterns.

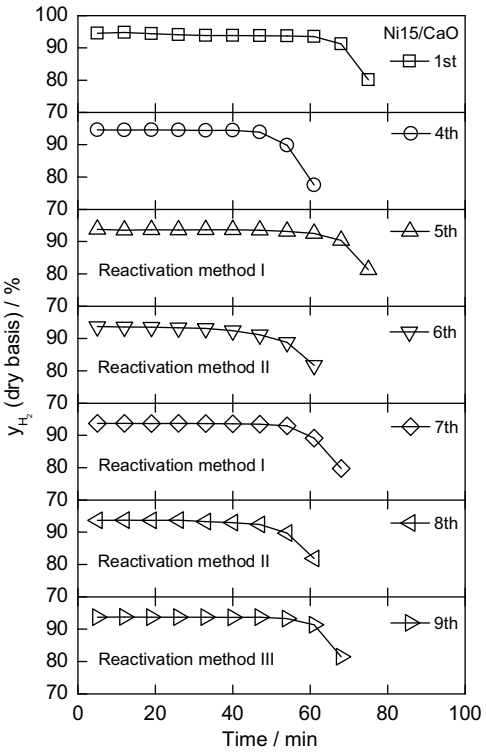

Fig. 14. H_2 concentration profiles over Ni15/CaO after reactivation by different methods: catalyst (4 g), 600 °C, 1 bar, H_2O/CH_4 (molar ratio) = 3, $F_{CH_4,in}$ = 16.6 mL/min.

edly increases the diffusion barrier of reactants to some active sites located in the interior of the catalyst particles and restricts the absorption of CO_2 by inner CaO grains, and hence degrades the catalyst performance.

Fig. 13(B) shows the Ca 2p and Zr 3d XPS spectra of fresh and 90-cycles used Ni15/CaZr, where the binding energies of the characteristic peaks agree with the literature data [52]. It is evident that the surface Ca/Zr atomic ratio of the used Ni15/CaZr is much higher than that of the fresh one, implying a possible migration of Ca from the inner region of the catalyst to the outer surface. Although Sun et al. [53] inferred that the outward diffusion of Ca^{2+} was of low possibility for the reaction of CaO and CO_2, but the presence of CH_4 and H_2O in the SMR reaction as well as the nickel species probably facilitates the diffusion process of Ca^{2+}, which in turn affects the catalyst structure. Indeed, as shown in Fig. 13(C), the diffraction peaks assigned to CaO become progressively weaker and broader with cycling, and the average crystallite sizes of CaO for fresh, 10-cycles used and 90-cycles used Ni15/CaZr are calculated to be 38.9, 28.6 and 20.4 nm, respectively, by using the Scherrer equation through line broadening of the CaO (200) peak ($2\theta = 37.4^\circ$). Although the CaO grains at the outer surface of the catalyst particles sinter, most grains inside the particles are very small (as indicated by the circle in Fig. 13(A)). The possibility of the loss of calcium species from the used catalyst is excluded by comparison of the composition of fresh Ni15/CaZr with that of used catalyst. The EDX analysis of the 90-cycles used Ni15/CaZr gives a composition of 47.2wt% Ca, 11.9wt% Zr and 13.9wt% Ni, which is in good accord with the composition of the fresh catalyst (48.6wt% Ca, 12.5wt% Zr and 15.0wt% Ni). With regard to Ni, its average crystallite size (determined by XRD) increases from 22.6 nm (fresh) to 26.3 nm (10-cycles used) and to 30.5 nm (90-cycles used), mainly due to the high temperature and the presence of steam in the SMR [54]. However, the average sintering rate of Ni over the last 80 cycles (0.2%/cycle) is only 1/8 that over the first 10 cycles (1.6%/cycle). On the other hand, the average crystallite size of $CaZrO_3$ slightly varies from 16.2 nm (fresh) to 18.5 nm (90-cycles used), demonstrating the excellent stability of this materials over the long-term service.

3.4. Reactivation of bifunctional catalysts

Ni15/CaO, because of its poor stability, is employed as a sample bifunctional catalyst to explore possible reactivation methods for the partially deactivated catalyst. Three methods are investigated: (I) hydration at low temperature: the partially deactivated catalyst is first calcined at 800 °C for 1 h under pure N_2 (100 mL/min) and then hydrated at 250 °C for 3 h in a stream of 50% H_2O/50% N_2 (100 mL/min); (II) calcination with steam at high temperature: the catalyst is calcined at 800 °C for 1 h in 50% H_2O/50% N_2 (100 mL/min); and (III) additional carbonation at mild temperature: the catalyst is first calcined at 800 °C for 1 h under pure N_2 (100 mL/min) and then carbonated at 650 °C for 3 h in 80% CO_2/20% N_2 (100 mL/min), followed by calcination at 800 °C for 1 h under pure N_2 (100 mL/min). Fig. 14 presents the H_2 concentration profiles obtained by different reactivation methods. It can be seen that the prebreakthrough period is reduced from around 60 min to 47 min during the first four cycles operated in mode II, after which the catalyst is reactivated by method I prior to the next carbonation. In the 5th cycle the duration of the prebreakthrough period returns to 60 min, indicating that the catalytic activity is restored. This is mostly caused by the hydration-derived cracks and channels in the catalyst particles, which in turn allow rapid diffusion of CO_2 to the particle interior and thus improve the CO_2 uptake [55]. Indeed, it is observed that reactivating the sintering Ni15/CaO (Fig. 15(A)) by method I produces many small grains and cracks (Fig. 15(B)). After the 5th cycle, the catalyst is reactivated by method II, showing a reduced prebreakthrough period at the 6th cycle (40 min), implying that the use of steam during calcination is detrimental to the catalyst, which is probably because steam at high temperature accelerates the sintering process of CaO [56,57]. The results of the following two cycles that are separately reactivated by method I (7th cycle) and method II (8th cycle) confirm the positive effect of method I and the negative effect of method II on reactivation of the catalytic activity. Finally, the 8-cycles used Ni15/CaO is reactivated by method III and the duration of the prebreakthrough period at the subsequent 9th cycle returns again to about 60 min, indicative of recovery of catalytic activity. The reason for this is connected with the extended carbonation time and the resulting increased CaO utilization, just as mentioned above. The morphology of the catalyst reactivated by method III (Fig. 15(C)) is also favorable in view of improved diffusion of reactants compared to the deactivated catalyst (Fig. 15(A)).

Although both method I and method III can effectively recover the catalytic activity of partially deactivated bifunctional catalyst, method III is more practically applicable considering the decreased mechanical stability of hydrated particles [58–60]. In the final part of this study, method III is therefore used to reactivate the promising but still partially deactivated Ni15/CaZr. As shown in Fig. 16, during the cyclic SESMR process operated in mode II, the prebreakthrough period is shortened from around 50 min at the first cycle to around 30 min at the 50th cycle, after which the catalyst is reactivated for the first time by method III and the prebreakthrough period is lengthened to 40 min at the 51th cycle. Then, the catalyst continuously experiences another 26 cycles and the prebreakthrough period is reduced again to about 30 min at the 77th cycle, but after reactivation for the second time the duration of this period returns immediately to around 40 min. Fig. 17 further

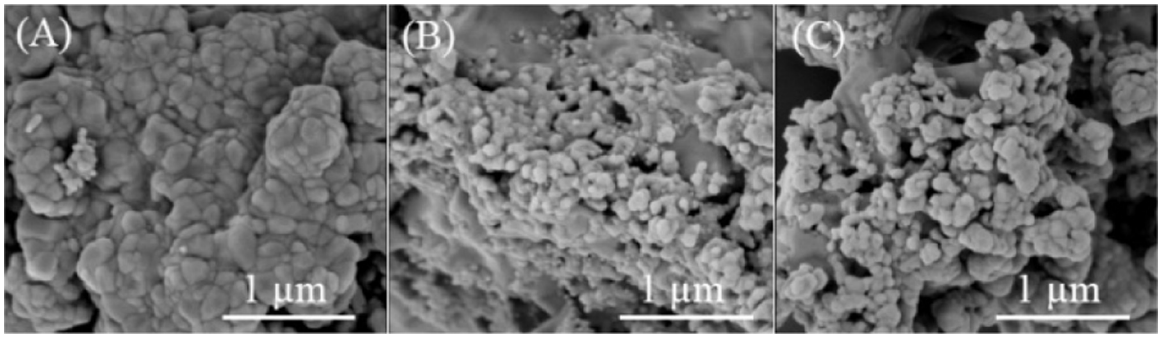

Fig. 15. FESEM images of (A) partially deactivated and (B, C) reactivated Ni15/CaO.

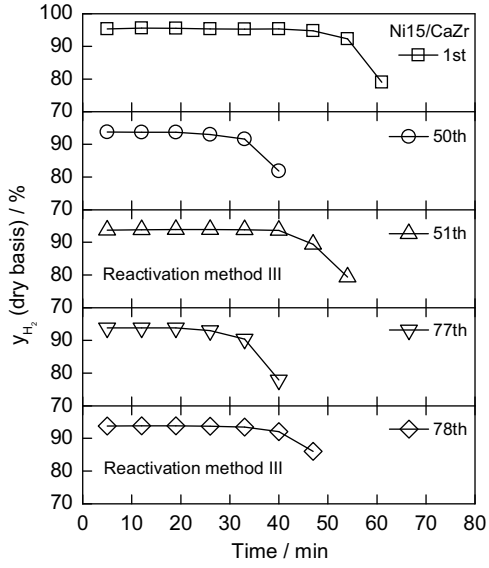

Fig. 16. H_2 concentration profiles over Ni15/CaZr before and after reactivation: catalyst (4 g), 600 °C, 1 bar, H_2O/CH_4 (molar ratio) = 3, $F_{CH_4,in}$ = 16.6 mL/min.

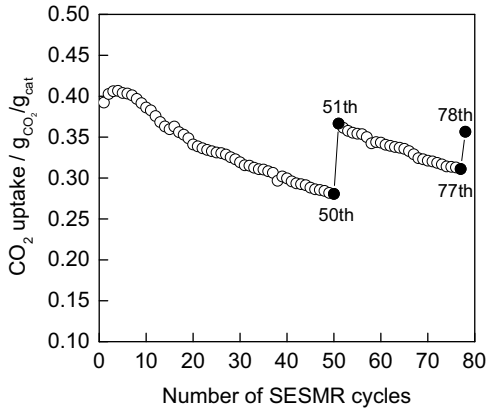

Fig. 17. CO_2 uptake of Ni15/CaZr before and after reactivation: catalyst (4 g), 600 °C, 1 bar, H_2O/CH_4 (molar ratio) = 3, $F_{CH_4,in}$ = 16.6 mL/min.

presents the CO_2 uptake of Ni15/CaZr during these SESMR cycles, which is calculated as follows:

$$CO_2\,\text{uptake (SESMR)} = \frac{\int_0^{t_r} \left(F_{CH_4,in} - F_{CH_4,out} - F_{CO,out} - F_{CO_2,out}\right) dt \times M_{CO_2}}{W_{cat}}, g_{CO_2}/g_{cat}$$

where $F_{CH_4,in}$ is the inlet molar flow rate of CH_4, $F_{CH_4,out}$, $F_{CO,out}$ and $F_{CO_2,out}$ are the outlet molar flow rates of CH_4, CO and CO_2, respectively, t_r is the SESMR reaction time at each cycle, M_{CO_2} is the molar weight of CO_2, and W_{cat} is the catalyst weight. During the first 50 cycles, the CO_2 uptake of Ni15/CaZr, after an initial increase due to the self-reactivation, is gradually decreased similarly to that observed in the TGA (Fig. 6), but the CO_2 uptake obtained from the SESMR is in general lower than that from the TGA, especially after the first 5 cycles (Fig. 6 vs. Fig. 17), which can be attributed to the aforementioned negative effect of high-temperature steam that is used in the SESMR. Corresponding to the twice reactivation, the CO_2 uptake of Ni15/CaZr increases, respectively, from 0.28 g_{CO_2}/g_{cat} (50th cycle) to 0.37 g_{CO_2}/g_{cat} (51th cycle), and from 0.31 g_{CO_2}/g_{cat} (77th cycle) to 0.36 g_{CO_2}/g_{cat} (78th cycle), demonstrating the activity recovery. These results clearly show that method III proposed in this study, i.e., an additional carbonation step employed during the cyclic operation, is an effective and feasible way to reactivate the partially deactivated bifunctional catalysts that are used for the SESMR process.

4. Conclusions

A series of Ni/CaO-$CaZrO_3$ bifunctional catalysts with different Ni loading and CaO content were prepared by a citrate-based sol-gel method and applied to the SESMR process. In contrast to Ni/CaO whose CO_2 uptake as well as catalytic activity in SESMR decreased rapidly with cycling, Ni/CaO-$CaZrO_3$ showed much higher stability in cyclic operation, mainly owing to the stabilization effect of $CaZrO_3$ that can retard the sintering of CaO particles. Among all the catalysts investigated, Ni15/CaZr (Ni:CaO:$CaZrO_3$ = 15:60.3:24.7 (wt%)) had the most balanced properties, such as small grains, narrow Ni particle size distribution and uniform elemental distribution, and thus exhibited the best SESMR performance in terms of activity, stability and duration of the prebreakthrough period. In an extended test up to 90 SESMR cycles over Ni15/CaZr, although the product composition approached the equilibrium composition, the prebreakthrough period was gradually shortened, indicating the partial deactivation of the catalyst. This was mainly caused by a compact shell that was formed on the catalyst surface, which increased the diffusion barrier of reactants and limited the CO_2 capture by inner CaO grains. The compact shell of the used Ni15/CaZr had a Ca content much higher than that of the fresh counterpart, which was probably due to the migration of Ca species from the inner region of the catalyst to the outer surface. In order to recover the activity of partially deactivated catalyst, three reactivation methods, namely hydration at low temperature (250 °C), calcination with steam at high temperature (800 °C) and additional carbonation at mild temperature (650 °C), were studied. The last method proved to be the best, which can effectively restore the duration of the prebreakthrough period during a long-term cyclic SESMR process.

Acknowledgements

Financial supports from the National Natural Science Foundation of China (21276076), the Program for New Century Excellent Talents in University (NCET-13-0801), the Fundamental Research Funds for the Central Universities (222201313011) and the "111" project (B08021) are gratefully acknowledged.

References

[1] D.P. Harrison, Ind. Eng. Chem. Res. 47 (2008) 6486–6501.
[2] S.A. Bhat, J. Sadhukhan, AIChE J. 55 (2009) 408–422.
[3] M.S. Yancheshmeh, H.R. Radfarnia, M.C. Iliuta, Chem. Eng. J. 283 (2016) 420–444.
[4] B.L. Dou, C. Wang, Y.C. Song, H.S. Chen, B. Jiang, M.J. Yang, Y.J. Xu, Renew. Sust. Energy Rev. 53 (2016) 536–546.
[5] J.R. Hufton, S. Mayorga, S. Sircar, AIChE J. 45 (1999) 248–256.
[6] Y. Ding, E. Alpay, Chem. Eng. Sci. 55 (2000) 3929–3940.
[7] G.H. Xiu, J.L. Soares, P. Li, A.E. Rodrigues, AIChE J. 48 (2002) 2817–2832.
[8] D.K. Lee, I.H. Baek, W.L. Yoon, Chem. Eng. Sci. 59 (2004) 931–942.
[9] Z.S. Li, N.S. Cai, J.B. Yang, Ind. Eng. Chem. Res. 45 (2006) 8788–8793.
[10] C.S. Martavaltzi, E.P. Pampaka, E.S. Korkakaki, A.A. Lemonidou, Energy Fuels 24 (2010) 2589–2595.
[11] M.M. Xie, Z.M. Zhou, Y. Qi, Z.M. Cheng, W.K. Yuan, Chem. Eng. J. 207-208 (2012) 142–150.
[12] M. Broda, V. Manovic, Q. Imtiaz, A.M. Kierzkowska, E.J. Anthony, C.R. Müller, Environ. Sci. Technol. 47 (2013) 6007–6014.
[13] A.L. García-Lario, M. Aznar, G.S. Grasa, R. Murillo, J. Power Sources 285 (2015) 90–99.
[14] G.H. Xiu, P. Li, A.E. Rodrigues, Chem. Eng. Sci. 58 (2003) 3425–3437.
[15] E.L.G. Oliveira, C.A. Grande, A.E. Rodrigues, Chem. Eng. Sci. 66 (2011) 342–354.
[16] C.H. Lee, S.Y. Mun, K.B. Lee, J. Power Sources 281 (2015) 158–163.
[17] J.A. Satrio, B.H. Shanks, T.D. Wheelock, Ind. Eng. Chem. Res. 44 (2005) 3901–3911.
[18] C.S. Martavaltzi, A.A. Lemonidou, Chem. Eng. Sci. 65 (2010) 4134–4140.
[19] N. Chanburanasiri, A.M. Ribeiro, A.E. Rodrigues, A. Arpornwichanop, N. Laosiripojana, P. Praserthdam, S. Assabumrungrat, Ind. Eng. Chem. Res. 50 (2011) 13662–13671.
[20] H.Z. Feng, P.Q. Lan, S.F. Wu, Int. J. Hydrogen Energy 37 (2012) 14161–14166.
[21] M. Broda, A.M. Kierzkowska, D. Baudouin, Q. Imtiaz, C. Copéret, C.R. Müller, ACS Catal. 2 (2012) 1635–1646.
[22] J.N. Kim, C.H. Ko, K.B. Yi, Int. J. Hydrogen Energy 38 (2013) 6072–6078.
[23] H.R. Radfarnia, M.C. Iliuta, Chem. Eng. Sci. 109 (2014) 212–219.
[24] P. Xu, Z.M. Zhou, C.J. Zhao, Z.M. Cheng, AIChE J. 60 (2014) 3547–3556.
[25] A.L. García-Lario, G.S. Grasa, R. Murillo, Chem. Eng. J. 264 (2015) 697–705.
[26] M.R. Cesário, B.S. Barros, C. Courson, D.M.A. Melo, A. Kiennemann, Fuel Process. Technol. 131 (2015) 247–253.
[27] W. Dietrich, P.S. Lawrence, M. Grünewald, D.W. Agar, Chem. Eng. J. 107 (2005) 103–111.
[28] H. Schmidt-Traub, A. Górak, Integrated Reactor and Separation Operations, Springer, Verlag, Berlin, 2006.
[29] A. Kapil, S.A. Bhat, J. Sadhukhan, AIChE J. 54 (2008) 1025–1036.
[30] J. Solsvik, H.A. Jakobsen, Chem. Eng. J. 178 (2011) 407–422.
[31] K.R. Rout, H.A. Jakobsen, Fuel Process. Technol. 106 (2013) 231–246.
[32] K.D. Dewoolkar, P.D. Vaidya, Energy Fuels 29 (2015) 3870–3878.
[33] P. Xu, Z.M. Zhou, C.J. Zhao, Z.M. Cheng, Catal. Today 259 (2016) 347–353.
[34] J. Blamey, E.J. Anthony, J. Wang, P.S. Fennell, Prog. Energy Combust. 36 (2010) 260–279.
[35] J.J. Yin, C. Zhang, C.L. Qin, W.Q. Liu, H. An, G. Chen, B. Feng, Chem. Eng. J. 198-199 (2012) 38–44.
[36] B. Arias, G.S. Grasa, M. Alonso, J.C. Abanades, Energy Environ. Sci. 5 (2012) 7353–7359.
[37] J.M. Valverde, P.E. Sanchez-Jimenez, L.A. Perez-Maqueda, M.A.S. Quintanilla, J. Perez-Vaquero, Appl. Energy 125 (2014) 264–275.
[38] C.J. Zhao, Z.M. Zhou, Z.M. Cheng, Ind. Eng. Chem. Res. 53 (2014) 14065–14074.
[39] S.G. Liu, L.X. Guan, J.P. Li, N. Zhao, W. Wei, Y.H. Sun, Fuel 87 (2008) 2477–2481.
[40] A.M. Kierzkowska, R. Pacciani, C.R. Müller, ChemSusChem 6 (2013) 1130–1148.
[41] V. Manovic, E.J. Anthony, Environ. Sci. Technol. 42 (2008) 4170–4174.
[42] S. Stendardo, L.K. Andersen, C. Herce, Chem. Eng. J. 220 (2013) 383–394.
[43] P.H. Chang, W.C. Huang, T.J. Lee, Y.P. Chang, S.Y. Chen, ACS Appl. Mater. Interfaces 7 (2015) 6172–6179.
[44] H. Lu, P.G. Smirniotis, F.O. Ernst, S.E. Pratsinis, Chem. Eng. Sci. 64 (2009) 1936–1943.
[45] P. Xu, M.M. Xie, Z.M. Cheng, Z.M. Zhou, Ind. Eng. Chem. Res. 52 (2013) 12161–12169.
[46] S.K. Bhatia, D.D. Perlmutter, AIChE J. 29 (1983) 79–86.
[47] G. Grasa, R. Murillo, M. Alonso, J.C. Abanades, AIChE J. 55 (2009) 1246–1255.
[48] Z.M. Zhou, P. Xu, M.M. Xie, Z.M. Cheng, W.K. Yuan, Chem. Eng. Sci. 95 (2013) 283–290.
[49] H.R. Radfarnia, M.C. Iliuta, Chem. Eng. Process. 86 (2014) 96–103.
[50] A.I. Lysikov, A.N. Salanov, A.G. Okunev, Ind. Eng. Chem. Res. 46 (2007) 4633–4638.
[51] B. Arias, J.C. Abanades, G.S. Grasa, Chem. Eng. J. 167 (2011) 255–261.
[52] R. Koirala, K.R. Gunugunuri, S.E. Pratsinis, P.G. Smirniotis, J. Phys. Chem. C 115 (2011) 24804–24812.
[53] Z.C. Sun, S.W. Luo, P.P. Qi, L.S. Fan, Chem. Eng. Sci. 81 (2012) 164–168.
[54] J. Sehested, Catal. Today 111 (2006) 103–110.
[55] R.W. Hughes, D. Lu, E.J. Anthony, Y.H. Wu, Ind. Eng. Chem. Res. 43 (2004) 5529–5539.
[56] R.H. Borgwardt, Ind. Eng. Chem. Res. 28 (1989) 493–500.
[57] F.C. Yu, N. Phalak, Z.C. Sun, L.S. Fan, Ind. Eng. Chem. Res. 51 (2012) 2133–2142.
[58] J. Blamey, N.P.M. Paterson, D.R. Dugwell, P.S. Fennell, Energy Fuels 24 (2010) 4605–4616.
[59] E.J. Anthony, Greenhouse Gas Sci. Technol. 1 (2011) 36–47.
[60] L. Zhang, B. Zhang, Z.Q. Yang, M.N. Guo, Energy Technol. 3 (2015) 10–19.